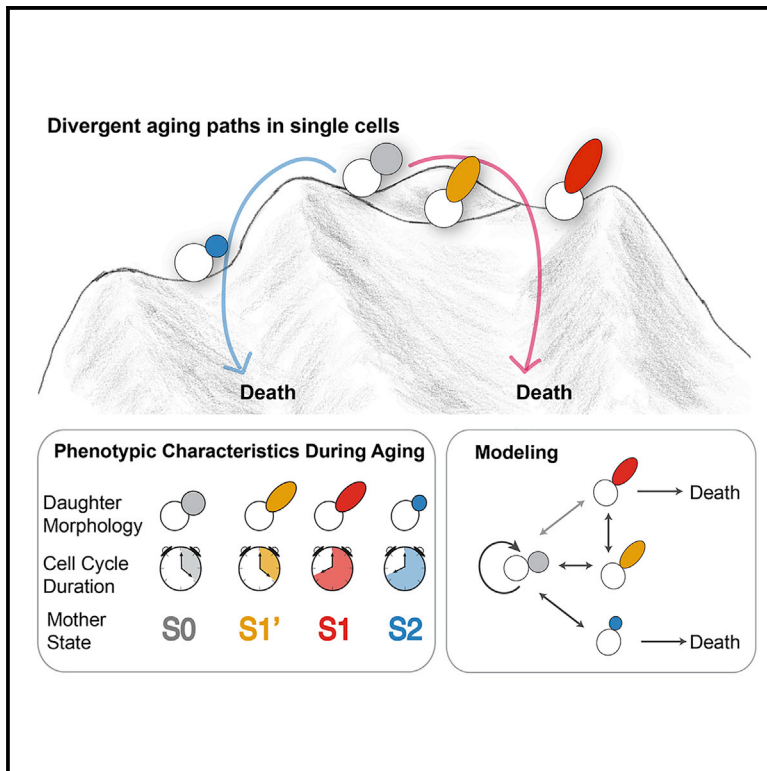# Divergent Aging of Isogenic Yeast Cells Revealed through Single-Cell Phenotypic Dynamics

Graphical Abstract

Highlights

- Single-cell phenotypic analysis reveals detailed replicative aging dynamics

- Isogenic cells differentiate early in life toward two distinct aging paths

- A stochastic state-transition model captures the landscape of aging dynamics

- Genetic and environmental factors modulate aging trajectories and kinetics

Authors

Meng Jin, Yang Li,
Richard O'Laughlin, ..., Lev S. Tsimring,
Jeff Hasty, Nan Hao

Correspondence

ltsimring@ucsd.edu (L.S.T.),
jhasty@eng.ucsd.edu (J.H.),
nhao@ucsd.edu (N.H.)

In Brief

Cellular aging is a complex, dynamic process. Even genetically identical cells age with distinct phenotypic changes and at different rates. What types of phenotypic changes occur during aging? How do these changes differ among individual aging cells? Can we modulate these changes to slow aging? We integrated microfluidics, single-cell imaging, and tracking with stochastic modeling to unravel the landscape through which isogenic cells can undergo distinct age-dependent phenotypic changes and progress through divergent aging paths.

CellPress

Cell Systems
Article

CellPress

Divergent Aging of Isogenic Yeast Cells Revealed through Single-Cell Phenotypic Dynamics

Meng Jin,[1] Yang Li,[2] Richard O'Laughlin,[3] Philip Bittihn,[1] Lorraine Pillus,[2,4] Lev S. Tsimring,[1,*] Jeff Hasty,[1,2,3,*] and Nan Hao[1,2,5,*]

[1]BioCircuits Institute, University of California, San Diego, La Jolla, San Diego, CA 92093, USA
[2]Section of Molecular Biology, Division of Biological Sciences, University of California, San Diego, La Jolla, San Diego, CA 92093, USA
[3]Department of Bioengineering, University of California, San Diego, La Jolla, San Diego, CA 92093, USA
[4]UCSD Moores Cancer Center, University of California, San Diego, La Jolla, San Diego, CA 92093, USA
[5]Lead Contact
*Correspondence: ltsimring@ucsd.edu (L.S.T.), jhasty@eng.ucsd.edu (J.H.), nhao@ucsd.edu (N.H.)
https://doi.org/10.1016/j.cels.2019.02.002

SUMMARY

Although genetic mutations that alter organisms' average lifespans have been identified in aging research, our understanding of the dynamic changes during aging remains limited. Here, we integrate single-cell imaging, microfluidics, and computational modeling to investigate phenotypic divergence and cellular heterogeneity during replicative aging of single *S. cerevisiae* cells. Specifically, we find that isogenic cells diverge early in life toward one of two aging paths, which are characterized by distinct age-associated phenotypes. We captured the dynamics of single cells along the paths with a stochastic discrete-state model, which accurately predicts both the measured heterogeneity and the lifespan of cells on each path within a cell population. Our analysis suggests that genetic and environmental factors influence both a cell's choice of paths and the kinetics of paths themselves. Given that these factors are highly conserved throughout eukaryotes, divergent aging might represent a general scheme in cellular aging of other organisms.

INTRODUCTION

Cellular aging is a complex, dynamic process driven by a wide variety of molecular and cellular damage (Kennedy et al., 2014). As a result, even genetically identical cells can age with distinct phenotypic changes and at significantly different rates. Previous studies have focused on identifying genes and factors that influence the average lifespan of a cell population (Guarente and Kenyon, 2000). However, the temporal dynamics of cellular changes during aging and how these dynamics differ among individual cells remain largely unclear. Careful investigations of single-cell aging dynamics, which hold the promise of tremendously advancing the mechanistic understanding of cellular aging, have long been hindered by technological challenges.

Recent developments in time-lapse imaging technologies have provided powerful tools for analyzing single-cell dynamics (Harton and Batchelor, 2017; Levine et al., 2013; Purvis and Lahav, 2013). In this study, we integrated advances in these technologies with stochastic modeling to investigate cellular aging processes and unraveled how isogenic cells undergo distinct age-dependent phenotypic changes and progress through divergent aging trajectories.

We chose the replicative aging of yeast *S. cerevisiae* as a model system to study the dynamics of single-cell aging. For over 50 years since its first analysis, yeast replicative aging has served as a genetically tractable model for the aging of mitotic cell types such as stem cells and has led to the identification of many well-conserved genetic and environmental factors that influence longevity throughout eukaryotes (He et al., 2018; Steinkraus et al., 2008). Similar to stem cells (Inaba and Yamashita, 2012), budding yeast cells divide asymmetrically: the mother cell keeps more volume than daughter cells, and cellular components are also partitioned unequally between the mother and daughter cells. As a result of this asymmetric segregation, aging-promoting factors, such as damaged proteins and aberrant genetic material, are believed to be primarily retained in the mother cell so that daughter cells can be rejuvenated and start a healthy life with full replicative potential (reviewed in Henderson and Gottschling, 2008 and Yang et al., 2015).

Replicative lifespan (RLS) is defined as the number of cell divisions of a mother cell before its death (Mortimer and Johnston, 1959). The conventional method for studying replicative aging in yeast involves the manual removal of daughter cells from mother cells after each division (Steffen et al., 2009), which is labor intensive and low throughput. Furthermore, it does not allow tracking of cellular changes during aging. Advances in microfluidic technology have enabled continuous live-cell measurements of aging mother cells and hence have made it possible to study the dynamics of physiological changes during single-cell aging (Chen et al., 2017).

We have recently reported the development of a microfluidic device that enables tracking of mother cells and each of their newborn daughters during their entire lifespan, thereby capturing the complete aging process (Li et al., 2017). Here, we combined this experimental platform with computational
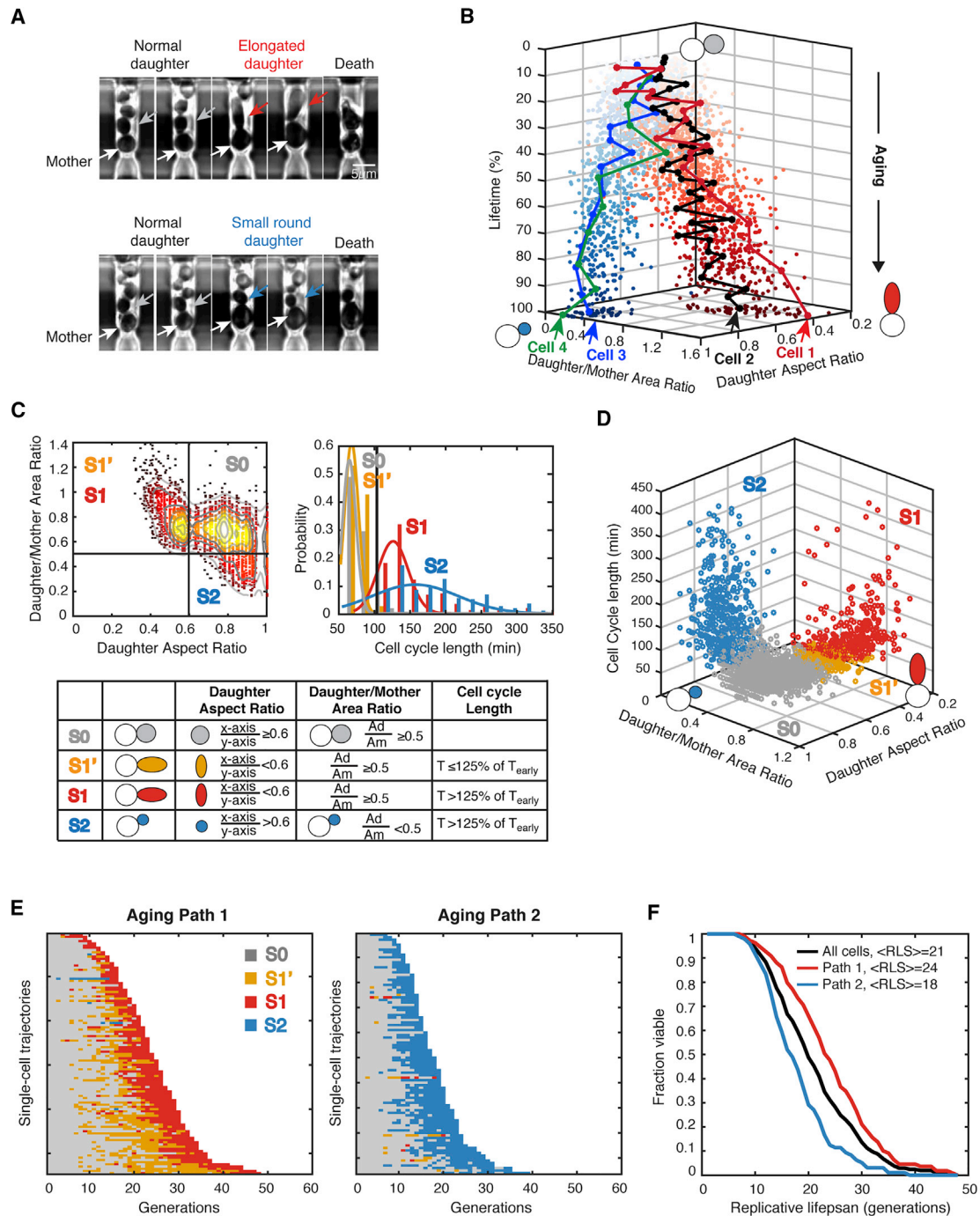
Figure 1. Single-Cell Phenotypic Analysis Reveals Two Divergent Aging Paths

(A) Representative images of cells illustrating two distinct types of morphological changes during replicative aging. Top row, a mother cell producing elongated daughters during aging; bottom row, a mother cell producing small round daughters during aging. White arrows point to mother cells. Gray arrows point to early normal daughters. Red arrows point to elongated daughters. Blue arrows point to small round daughters.

(B) Representative single-cell aging trajectories along two diverged paths toward cell death. Each dot represents the morphology state (daughter/mother area ratio; daughter aspect ratio) of an aging mother cell at one cell division. The z axis shows the percentage of lifetime. Four representative single-cell trajectories are shown: cell 1 and cell 2 are moving along the path with elongated daughters (red dots), while cell 3 and cell 4 are moving along the path with small round daughters (blue dots). The distance between two adjacent dots in one single-cell trajectory represents the length of this cell division. Arrows indicate the points of cell death.

(C) Categorization of age-dependent phenotypic conditions into four states. Daughter/mother area ratio, daughter aspect ratio, and cell-cycle length have been measured for each aging mother cell at each cell division. Thresholds used to define states are indicated by black lines. Top left panel, the distribution of daughter aspect ratio versus daughter/mother area ratio. Top right panel, the distributions of cell-cycle lengths. Bottom panel, the definitions of the four states (S0, S1', S1, and S2) based on the three quantified phenotypic metrics. T_{early}, the mean cell-cycle length of the first 25% of lifespan. See also Figure S8.

(legend continued on next page)

modeling to analyze the heterogeneous aging dynamics in single yeast cells and to examine how distinct genetic and environmental factors regulate these dynamics.

RESULTS

Early-Life Divergence of Isogenic Cells toward Two Distinct Aging Paths

Using a recently developed microfluidic device and time-lapse microscopy, we tracked the phenotypic changes of isogenic yeast cells during aging in a well-controlled and constant environment. A unique feature of our device is the long finger-shaped chamber that can trap the mother cell throughout its entire lifespan, which specifically allows monitoring daughter cells for at least one cell cycle (Li et al., 2017). This design provides important information about the sizes and morphologies of newborn daughter cells, which could reflect the physiological state of their mother cell at different ages. We observed heterogeneous phenotypic changes during the aging process of isogenic cells. Some cells, during aging, continuously produced daughter cells with a characteristic elongated morphology until death, whereas the other cells, during later stages of aging, produced small round daughters with sharply increased cell-cycle length (Figure 1A).

To quantitatively analyze the dynamic changes during single-cell aging, we measured three phenotypic metrics for each mother cell at each of its divisions: the aspect ratio of width and height for elliptical fit of the daughter cell, the area ratio between daughter and mother cells, and the cell-cycle length. We performed this quantification for a total of 205 wild-type (WT) mother cells throughout their entire lifespans. We tracked the age-dependent changes of these phenotypic metrics in individual mother cells and found two highly divergent aging paths: one path moves toward decreasing aspect ratios of daughters (elongated daughter morphology) until death, whereas the other path progresses toward lower daughter/mother area ratios (small round daughter). The majority of cells entered one of these two paths quite early in their life and proceeded along the selected path toward their final death (see representative cell trajectories in Figure 1B; Videos S1 and S2).

Based on the distributions of the three phenotypic metrics, we further categorized the age-dependent phenotypic conditions into four discrete states (Figures 1C and 1D). State 0 (S0) is the initial state of young mother cells, characterized by producing round daughter cells with sizes comparable to that of the mother cell (aspect ratio $\geq$ 0.6; daughter/mother area ratio $\geq$ 0.5). State 1 (S1) is the state when a mother cell produces elongated daughters (aspect ratio < 0.6; daughter/mother area ratio $\geq$ 0.5) and the cell cycle becomes significantly longer (>125% of the mean cell-cycle length of the first 25% of lifespan). Between S1 and S0, we also defined state 1' (S1'), where a mother cell produces an elongated daughter cell, but the cell-cycle length is similar to that of S0 state ($\leq$125% of the mean cell-cycle length of the first 25% of lifespan). State 2 (S2) is the state

when a mother cell goes through significantly extended cell cycle (>125% of the mean cell-cycle length of the first 25% of lifespan) and gives birth to a small round daughter (aspect ratio $\geq$ 0.6; daughter/mother area ratio < 0.5). These thresholds for state distinction are chosen according to inherent features of the distributions of daughter aspect ratio, daughter/mother area ratio, and cell cycle duration, as shown in Figure 1C (see Quantification of Phenotypic Metrics in the STAR Methods for more details).

We plotted the state-transition traces for all aging mother cells in Figure 1E. About 51% (104 out of a total of 205 cells) of cells first transition back and forth between S0 and S1' during the early phase of aging and then proceed to a more frequent S1' state and eventually a consecutive S1 phase until death (defined as "aging path 1"; Figure 1E, left). In contrast, 41% (83 out of a total of 205 cells) of cells never transition to S1' or S1 in the whole life; instead, these cells switch directly from S0 to a consecutive S2 state at the intermediate aging phase (defined as "aging path 2"; Figure 1E, right). Intriguingly, the vast majority of cells make their fate decisions at early ages. The decision between two aging paths occurs as early as the first transition to S1' or S2, within 5–10 divisions after birth. Once the decision has been made, most cells will proceed through this path until death, though a small fraction of cells did undergo cross-path transitions. About 6% (13 out of a total of 205 cells) of cells showed occasional transitions to S1' or S1 before switching to the consecutive S2 state, while 2% (5 out of a total of 205 cells) of cells experienced S2 before committing to aging path 1 (Figure 1E). These results indicate that fate switching is possible but rare. For simplicity, we categorized this small fraction of cross-path cells into path 1 or 2 based on their terminal states.

The two aging paths result in different average lifespans. Aging path 1 has a longer lifespan than aging path 2 (Figure 1F, 24 versus 18). Hence, cells moving along aging path 1 are more likely to be longer lived than path 2 cells. In addition, lifespan is also influenced by the state-transition kinetics during aging. We observed that among path 1 cells, longer-lived cells usually have a longer S0/S1' (gray/orange in Figure 1E) phase, while the later sustained S1 (red in Figure 1E) phase remains relatively constant among cells. This observation suggested that the transition between S0 and S1' delays a cell's entry into the consecutive S1 phase and hence is highly correlated with the final lifespan (Figure S1). For path 2 cells, a longer lifespan is often associated with a later switching to S2. Therefore, the divergence of aging trajectories and the variance in state-transition kinetics, together, contribute to the heterogeneity in lifespans of isogenic cells.
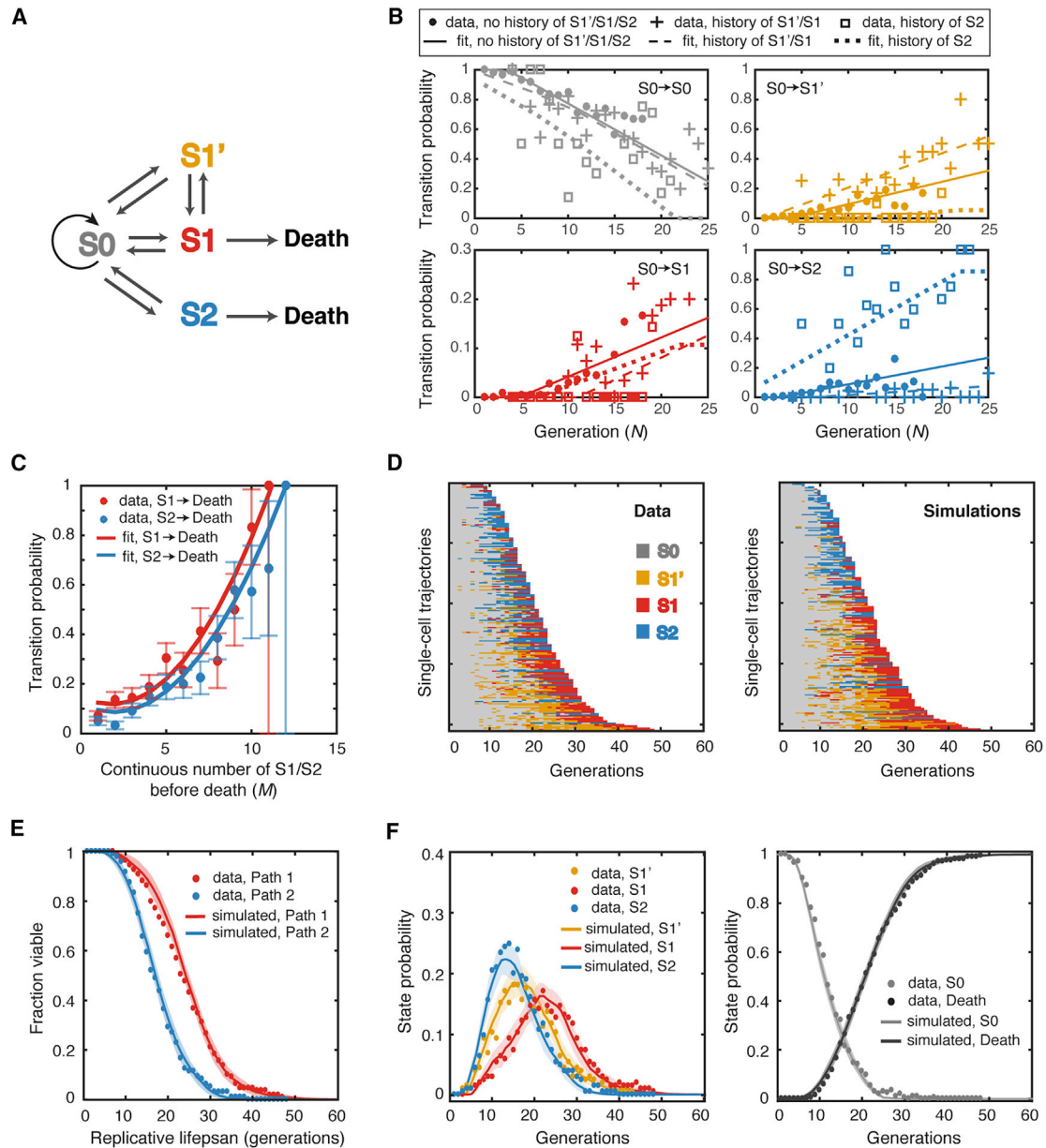
A Stochastic Discrete-State Model for Single-Cell Aging

To establish a quantitative framework for understanding heterogeneous aging processes, we developed a stochastic discrete-state model for single-cell aging (Figure 2A). Based on the phenotypic measurements and quantifications described in Figure 1, our model assumes that a cell can be in one of the four

(D) Distributions of the four states within the 3D phenotypic metric space.

(E) Single-cell state-transition trajectories along two distinct aging paths. Each row represents the time trace of a single cell throughout its lifespan. Cells are sorted by their lifespans. Colors represent their cellular states: S0, gray; S1', orange; S1, red; and S2, blue. Aging path 1 (left), cells transitioned through S0, S1', and S1 (n = 109); aging path 2 (right), cells transitioned through S0 and S2 (n = 96).

(F) Replicative lifespans of two aging paths. Aging path 1, red; aging path 2, blue; and combined, black.

Figure 2. A Stochastic Model for Phenotypic State Transitions during Aging

(A) Schematic diagram of the discrete-state model. The transitions between states are indicated by arrows.

(B) Transition probabilities deduced from data fitting. The fractions of all cells at S0 of a given generation N that switch to S0, S1', S1, or S2 at the next cell cycle (gray, yellow, red, and blue solid circles, respectively) have been computed as a function of age (N). The transition probabilities for S0 cells with the experience of only S0 (no history), the most recent experience of S1'/S1 (history of S1'/S1), or S2 (history of S2) have been calculated separately. The best linear fits are shown by lines with the same color. See also Figures S2, S4, and S9 and Table S1.

(C) The transition probabilities from S1 or S2 to death deduced from data fitting. Solid circles represent the fractions of cells that died exactly after M consecutive generations in S1 or S2 over the total number of cells that lived for at least M consecutive generations in S1 or S2 (red, S1; blue, S2). Red and blue curves are best fits of these data using polynomial functions of M. The error bars indicate the expected standard deviation, as described in STAR Methods, Computational Modeling. See also Figures S3 and S10.

(D) Single-cell state-transition trajectories from the data (205 cells) (left), and from stochastic simulations (right). Each row represents the time trace of a single cell throughout its lifespan.

(E) The lifespans of two aging paths from simulations (red and blue curves) in comparison with experimental data (red and blue solid circles). Simulated lifespans were averaged from 50 simulations, each with 205 cells. Standard deviations of simulations are shown by shaded areas.

(F) Age-dependent state distributions of S1', S1, and S2 (left panel) and S0 and death (right panel). Solid circles represent the experimental data. Solid curves represent simulated results averaged from 50 simulations, with shaded areas showing standard deviations of simulations.

states, S0, S1', S1, and S2, at each age. A newborn mother cell always starts from S0 and switches to other states during aging. Transition from state Si to Sj is stochastic and described by the transition probability p_{ij} that depends on the cell age. For example, $p_{01}(N)$ indicates the probability to switch from S0 to S1 at the age N. Our experimental data suggest that $p_{01'}$, p_{01}, and p_{02} all increase with replicative age, whereas p_{00} (the probability of remaining at S0) decreases with age. In addition, from the data, we did not observe any direct transitions between S1' and S2 or between S1 and S2, so we set those transition probabilities at zero. Finally, based on the data, we assume that an extended S1 or S2 phase can lead to cell death, the probabilities of which depend on the number of consecutive divisions (M) in either state.

To deduce the transition probabilities from the single-cell data, we computed the fraction of all the cells at Si (i = 0, 1', 1, and 2) of a given age that switch to Sj (j = 0, 1', 1, and 2) at the next cell cycle. As these data showed, the probability of staying at S0 decreases linearly with age, whereas the probability of transitioning from S0 to other states increases linearly with age (Figure 2B). To accurately simulate the experimental data, we found it necessary to separately compute the transition probabilities from S0 to Sj (j = 0, 1', 1, and 2) depending on the previous history that cells in state S0 have experienced. In this context, we consider cells to have a "history of S1'/S1" if their most recent state excursion from the S0 state was to states S1' or S1. Similarly, we define cells in state S0 as having a "history of S2" if their most recent excursion from S0 was to state S2. Cells that are in state S0 with a history of S1'/S1 have a higher transition probability to switch to S1' or S1 than cells currently in S0 but with a different history (Figure 2B, panels for S0 → S1' and S0 → S1). Conversely, cells with a history of S2 are significantly more likely to transit from S0 back to S2 compared to cells with a history of S1' or S1 (Figure 2B, panel for S0 → S2). In our model, we found that it is sufficient to recapitulate the history effects on current S0 cells by only considering the most recently visited state other than S0 (S1'/S1 and S2) and without considering the time that has passed since. Using linear regression, we approximated three sets of p_{00}, $p_{01'}$, p_{01}, and p_{02}, based on their histories, by linear functions of replicative age N (Figure 2B, with only experience of S0, with the most recent experience of S1'/S1, or S2; Figure S2). To keep assumptions minimal, we did not consider the history effects for other transition probabilities and hence computed only a single set of values for $p_{1'0}$, $p_{1'1'}$, $p_{1'1}$, p_{10}, $p_{11'}$, p_{11}, p_{20}, and p_{22} (Figure S2, all of the transition probabilities in WT). Furthermore, we calculated the fraction of cells that die after M consecutive divisions in S1 or S2. The fraction of cell death elevates dramatically as M increases. We approximated the probability of transition to death from S1 or S2 by a second-order polynomial function of M (Figures 2C and S3A).

Using the transition probabilities from fitting, we performed stochastic simulations using our discrete-state model. The simulations generated single-cell state trajectories (Figure 2D) that faithfully reproduce the single-cell data from experiments (Figure 1E). The simulations also quantitatively captured the statistical properties of age-dependent state transitions within an aging population, including the average lifespans for aging path 1 and 2 (Figure 2E) and the fractions of cells at each state during aging (Figure 2F). The age-dependent state distributions (Figure 2F)

confirmed that the cells started to switch from S0 to either S1' or S2 at about 5–10 divisions after birth. During this phase of life, through these transition events, cell fates are determined and diverge between two different aging paths toward death. Furthermore, from the model simulations, very few cells switch their paths in the middle of their lifespan because of two reasons: first, the two paths appear largely irreversible because of rapidly decreasing probabilities of transitioning back to S0 during aging, and second, individual cells' histories further bias cells to stay in the same path. It is important to note that without the assumption of history-dependent transition probabilities from S0, the model produced switching frequencies between two paths significantly higher than those observed experimentally (Figure S4A). Therefore, the history effect is critical for the early fate decision described above and thus for the divergence of the two aging paths.

In summary, our simple discrete-state model is sufficient to reproduce the observed heterogeneous dynamics of the single-cell aging process. We next set out to use this model to investigate how genetic and environmental perturbations affect state transitions during aging and thereby influence lifespan.

Sir2 Primarily Regulates the State-Transition Kinetics in Aging Path 1

We first examined the effect of $sir2\Delta$ mutants. SIR2 is the best-studied longevity gene to date, conserved from bacteria to humans. It encodes a lysine deacetylase that controls chromatin silencing and gene expression at various genomic sites (Gartenberg and Smith, 2016). We measured and quantified age-dependent phenotypic changes in $sir2\Delta$ cells. The $sir2\Delta$ cells showed all of the four states identified in aging WT cells, although the average lifespan is significantly shortened compared to that of WT (12 versus 21 divisions). As shown in Figure 3A, the absence of SIR2 increased the fraction of cells that experience aging path 1 (142 cells in path 1 and 46 cells in path 2), reduced the appearance of S1', and generally accelerated the transitions from S0 to other states.

We computed and fit the transition probabilities of the $sir2\Delta$ mutant at different cellular ages. Compared to that of WT, the transition probability from S0 to S1' is significantly reduced, with or without a history of S1'/S1, whereas the transition probability from S0 to S1 becomes clearly elevated (Figure S5, all of the transition probabilities in $sir2\Delta$). The probability of transition from continuous S1 to death is also increased (Figure S3B). With these transition probabilities obtained from experimental data in $sir2\Delta$, stochastic simulations reproduced the single-cell trajectories and the statistical properties of the aging population of $sir2\Delta$ cells (Figures 3A–3C).

Our modeling simulations revealed that $sir2\Delta$ can increase the fraction of cells going through aging path 1 because of a higher transition probability from S0 to S1, and at the same time, $sir2\Delta$ can reduce the appearance of S1' cells by decreasing the transition probability from S0 to S1'. In WT, most cells transitioning through aging path 1 will first switch back and forth between S0 and S1' for multiple cycles and then enter the consecutive S1 phase. In contrast, most $sir2\Delta$ cells will skip or shorten the intermittent S1' phase and shortcut directly to the S1 phase (Figures 3A and 3C). Therefore, aging path 1 in $sir2\Delta$ is accelerated toward death, resulting in a significantly shortened lifespan of
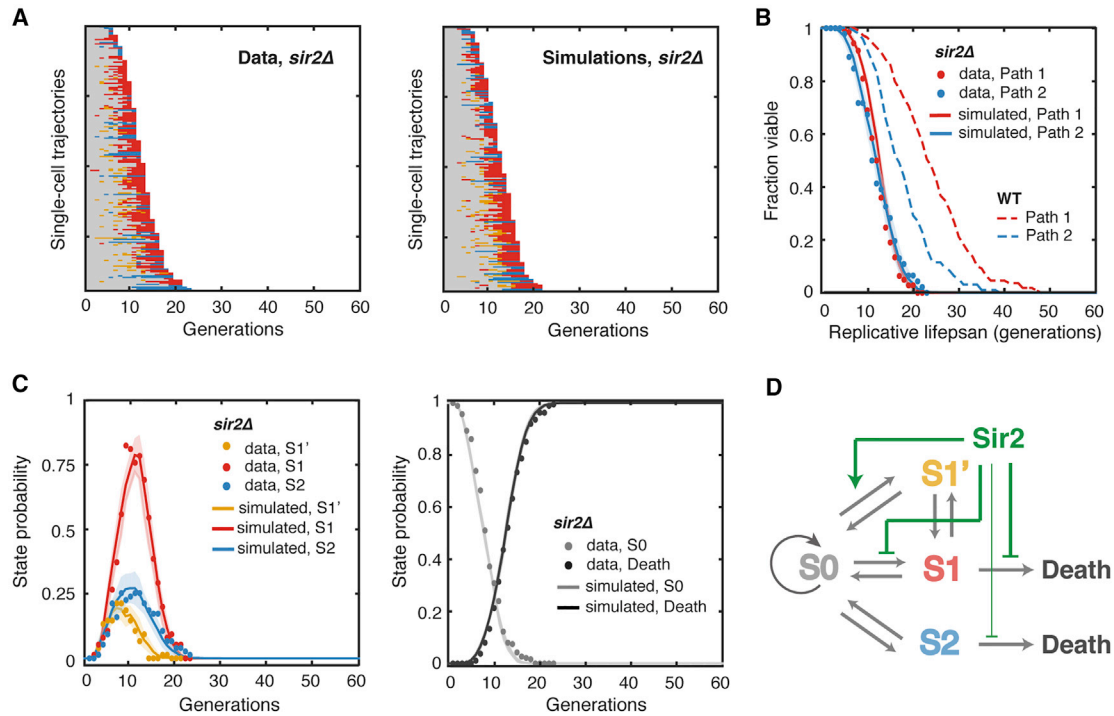
Figure 3. Aging-Dependent State Transitions in the Short-Lived *sir2Δ* Mutant

(A) Single-cell state-transition trajectories of *sir2Δ* from the data (188 cells, 142 in path 1 and 46 in path 2) (left), and from stochastic simulations (right).

(B) The lifespans of two aging paths in *sir2Δ* from experimental data (red and blue solid circles) and from simulations (red and blue curves). Dashed curves are the WT lifespans from Figure 1F for comparison.

(C) Age-dependent state distributions of S1', S1, S2, S0, and death in *sir2Δ*. Solid circles represent the experimental data. Solid curves represent simulated results averaged from 50 simulations, with shaded areas indicating standard deviation.

(D) Schematic diagram illustrates the effects of Sir2 at specific state-transition steps.

See also Table S1 and Figures S4, S5, and S9.

path 1 cells (Figure 3B, comparing solid and dashed red curves). These results raise the possibility that the transition to S1' might serve to signal as a damage-rescue process, which is partially dependent on Sir2. Mother cells, at intermediate phases of aging, may occasionally segregate some cellular damage to daughters, coinciding with an abnormally elongated morphology of these daughter cells, and thereby temporarily alleviate damage accumulation in mother cells and slow their aging.

Taken together, these findings from our single-cell data and model simulations suggest that Sir2 primarily regulates the state-transition kinetics in aging path 1. In particular, Sir2 slows aging by promoting the transition to S1', a potential rescue state, and also functions by repressing the transitions to S1 and to death (Figure 3D).

Sgf73 Ensures the Early-Life Divergence of the Two Aging Paths

Having tested the effect of the short-lived *sir2Δ* mutant on state transitions during aging, we next considered *sgf73Δ*, a long-lived mutant with the most extended lifespan ever reported (McCormick et al., 2015). *SGF73* is the yeast ortholog of human ataxin-7 (Mal, 2006), the gene that causes the neurodegenerative disease spinocerebellar ataxia type 7. *SGF73* encodes a histone deubiquitinase module component of the SAGA/SLIK complexes that control the expression of numerous genes

(Köhler et al., 2008; Lee et al., 2009). *SGF73* has been found to regulate many aging-related processes, including rDNA recombination, subtelomeric silencing, and asymmetric segregation of rDNA circles (Denoth-Lippuner et al., 2014; Mason et al., 2017; McCormick et al., 2014).

We tracked the phenotypic changes of the *sgf73Δ* cells during aging and found that these cells, similar to WT, showed all four states. However, their times in S1', S1, and S2 became much more intermittent, compared to those in aging WT cells. Interestingly, we observed that the two aging paths were less divergent, and the mutant cells would continue to switch between the two paths more frequently until late in their life (Figure 4A, left, 93 cells in path 1 and 67 cells in path 2). Compared with WT cells, a larger fraction (11% in *sgf73Δ* versus 6% in WT) of *sgf73Δ* cells transitioned to S1' or S1 before switching to continuous S2 and death (17 out of a total of 160 *sgf73Δ* cells). Similarly, more cells (8% in *sgf73Δ* versus 2% in WT) showed transient transitions to S2 before entering the terminal S1 state (13 out of a total of 160 *sgf73Δ* cells). This cannot be simply explained by increased cell division numbers in *sgf73Δ* cells. Instead, the history dependence in transition rates from S0 to other states is the dominating factor for the high switching frequencies (Figures S6 and S4C).

We computed and fit the transition probabilities of *sgf73Δ* and found that the transition probabilities from S1', S1, and S2 back to S0 decreased much more slowly with age in the mutant compared
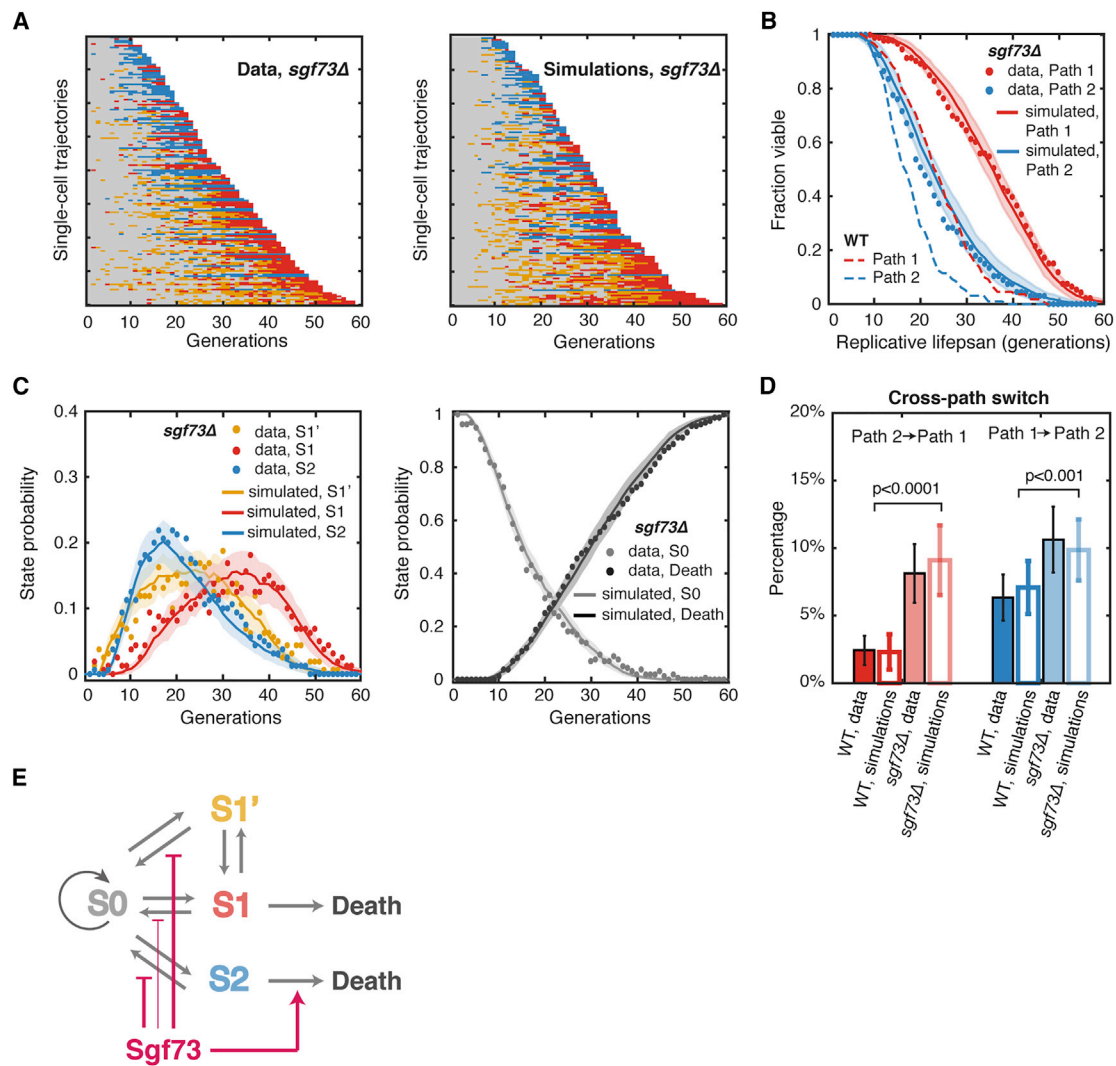
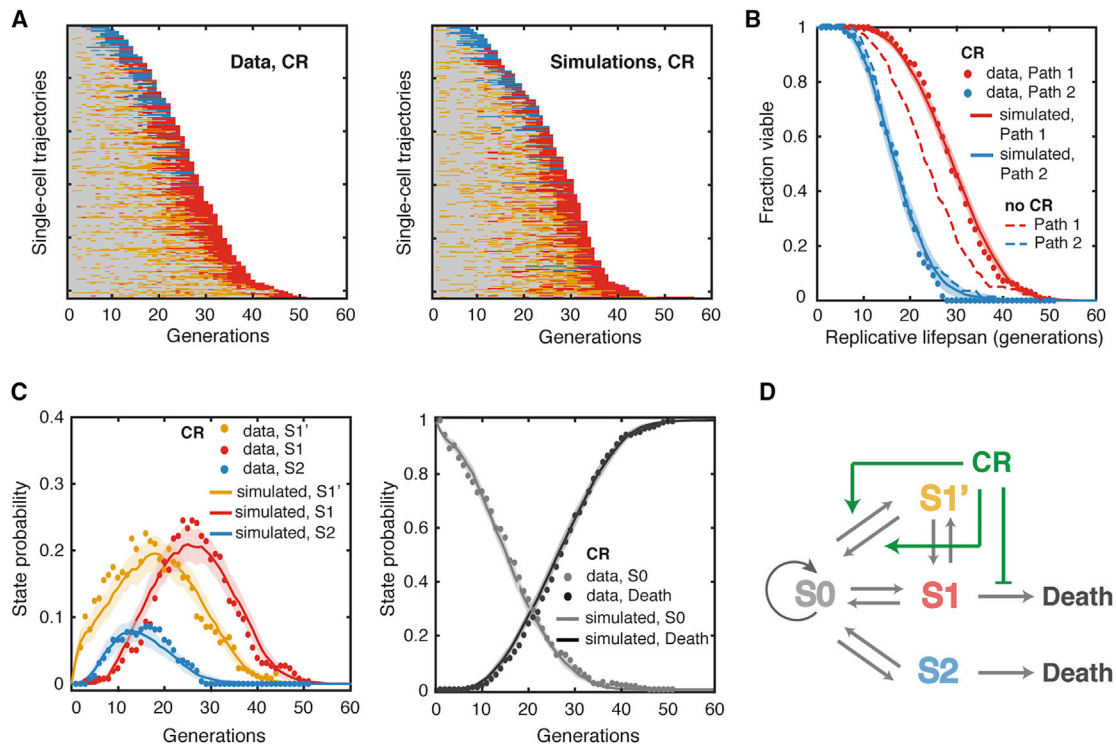**Figure 4. Aging-Dependent State Transitions in the Long-Lived *sgf73Δ* Mutant**

(A) Single-cell state-transition trajectories of *sgf73Δ* from the data (160 cells, 93 in path 1 and 67 in path 2) (left) and from stochastic simulations (right).

(B) The lifespans of two aging paths in *sgf73Δ* from experimental data (red and blue solid circles) and from simulations (red and blue curves). Dashed curves are the WT lifespans from Figure 1F for comparison.

(C) Age-dependent state distributions of S1', S1, S2, S0, and death in *sgf73Δ*. Solid circles represent the experimental data. Solid curves represent simulated results averaged from 50 simulations, with the shaded areas showing the standard deviations of simulations.

(D) Cross-path switching frequency in WT and *sgf73Δ*, calculated as a percentage of the total number of cells. Solid bars represent experimental data, with error bars indicating expected standard deviation (details see STAR Methods, Computational Modeling). Open bars represent simulations, with error bars indicating standard deviation of 50 simulations. p < 0.001 for both paths with two-sample t test. See also Table S1 and Figures S4, S6, S9, and S10.

(E) Schematic diagram illustrates the effects of Sgf73 at specific state-transition steps.

to that of WT. In addition, the previous history had a weaker influence on the transition probabilities from S0 to S1' or S1 (Figure S6, all of the transition probabilities in *sgf73Δ*). These two changes together contribute to more frequent reverse transitions and even switching between the aging paths. Furthermore, the transition probability from continuous S2 phase to death became dramatically reduced in the mutant (Figure S3C). Consistently, our simulations showed that *sgf73Δ* did not postpone the onset of transitions to S1', S1, or S2. Instead, as a result of more frequent reverse transitions and delayed cell death, the induction of cell fractions in these states lasted longer, resulting in an

extended lifespan (Figures 4B and 4C). The simulation showed higher possibilities of cross-path state transitions in *sgf73Δ*, consistent with the experimental observations (Figure 4D).

These results from the *sgf73Δ* mutant revealed that Sgf73 promotes aging through at least two mechanisms (Figure 4E). First, Sgf73 inhibits the reverse transition steps to S0 and thus re-presses cross-path transitions, which functions to ensure an early-life differentiation of individual cells with accelerated pro-gression toward distinct aged states (S1 or S2). Second, once cells enter the S2 state, Sgf73 also expedites the progression to cell death.

Figure 5. Aging-Dependent State Transitions under CR

(A) Single-cell state-transition trajectories under CR from the data (257 cells, 192 in path 1 and 65 in path 2) (left) and from stochastic simulations (right).

(B) The lifespans of two aging paths under CR from experimental data (red and blue solid circles) and from simulations (red and blue curves). Dashed curves are the WT lifespans under the glucose-rich conditions from Figure 1F for comparison.

(C) Age-dependent state distributions of S1', S1, S2, S0, and death under CR. Solid circles represent the experimental data. Solid curves represent simulated results averaged from 50 simulations, with shaded areas indicating standard deviation. See also Table S1 and Figures S4, S7, and S9.

(D) Schematic diagram illustrates the effects of CR at specific state-transition steps.

Caloric Restriction Promotes the Potential Rescue State S1'

Caloric restriction (CR) is the most robust intervention that extends lifespan in a wide range of organisms from yeast to mammals (Colman et al., 2009; Fontana et al., 2010; Lakowski and Hekimi, 1998; Partridge et al., 2005). However, the mechanisms underlying how CR, or environmental factors in general, influence aging-related processes remain obscure. Having examined the roles of genetic factors as described above, we now applied our approach to CR, to evaluate its effects on aging dynamics.

We found that under CR (0.05% glucose), the majority of aging cells displayed an earlier and highly extended intermittent S1' phase (Figure 5A, left). As a result, a much larger fraction of cells went through aging path 1 than path 2 (75% in path 1, 192 cells versus 25% in path 2, 65 cells), significantly different from aging under nutrient-rich conditions (Figure 1E, left). In addition, the occurrence of the subsequent S1 phase and death in these cells was dramatically delayed, leading to a significantly extended lifespan of path 1 cells. In contrast, the lifespan of path 2 cells was not affected (Figure 5B). We further computed transition probabilities and performed stochastic simulations. In agreement with the observations from single-cell data, the transition from S0 to S1' occurred much earlier and more frequently under CR and lasted much longer, resulting in a delayed accumulation

of cells in S1 (Figures 5C and S7, all of the transition probabilities under CR). The transition from S1 to death is also delayed under CR (Figure S3D). At the same time, because of the competition from the early increased transition to S1', the transition probability from S0 to S2 became much lower (Figures 5C and S7A), and even among the cells with the terminal S2 state, ~58% of them experienced S1' state early in their life (38 out of 65 cells ended in path 2) (Figure 5A, left). Therefore, CR regulates the aging dynamics primarily by promoting S1', which biases cells toward a slowed aging path 1 (Figure 5D).

These results are in support of our postulation that S1' might serve as a potential rescue state that slows aging. Whereas the occurrence of S1' is reduced in the short-lived *sir2Δ* mutant (Figure 3), it becomes much more frequent in *sgf73Δ* and under CR (Figures 4 and 5), both of which extend longevity. This correlation between S1' and lifespan also holds true with measurements from single cells. Throughout isogenic populations tested in our study, individual cells with more frequent transitions to S1' tend to have a longer lifespan (Figure S1).

Model Prediction and Experimental Validation

To further challenge our model, we wanted to see whether the model can capture all essential aspects of the aging dynamics in a condition it has not previously seen. In our model, the final lifespan of a cell largely depends on how late a cell enters the
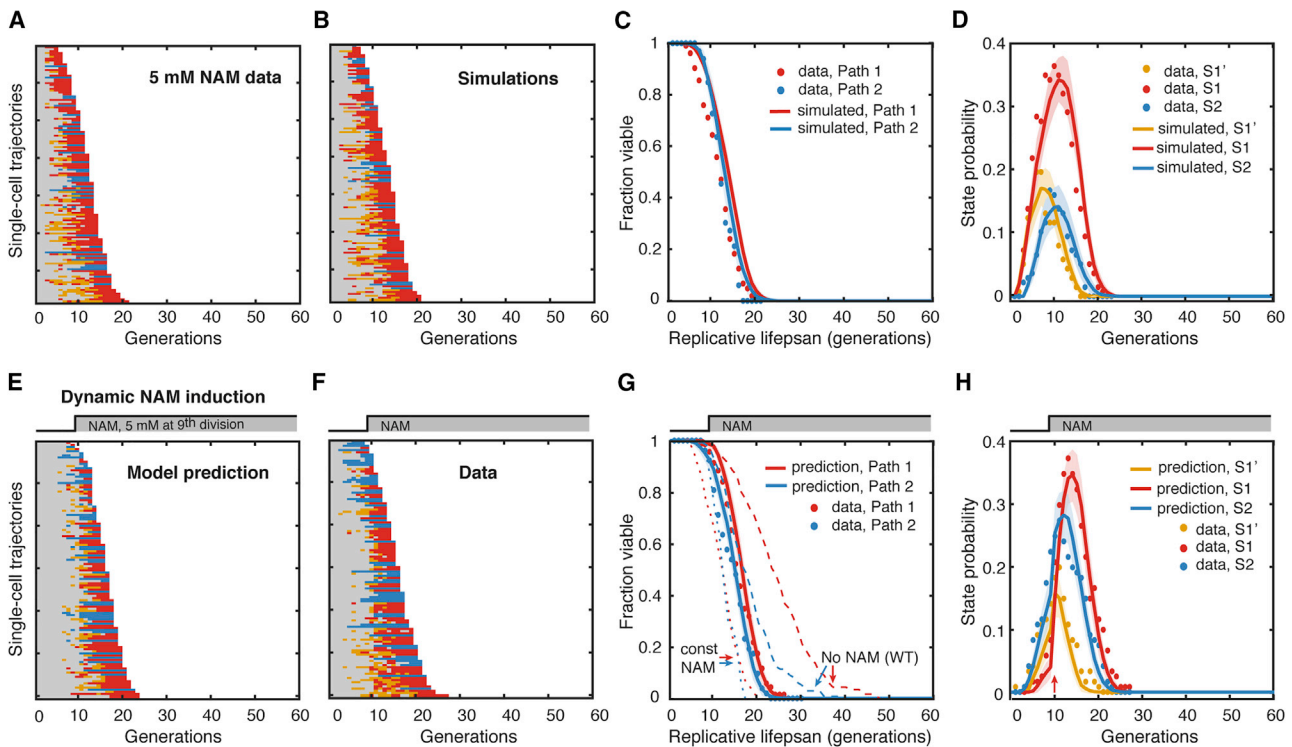
Figure 6. Model Prediction and Validation for a Dynamic Perturbation of Aging

(A and B) (A) Single-cell state-transition trajectories under 5 mM constant NAM from the data (137 cells with 104 in path 1 and 33 in path 2) and (B) from stochastic simulations.

(C) The lifespans of two aging paths under 5 mM constant NAM from experimental data (red and blue solid circles) and from simulations (red and blue curves).

(D) Age-dependent state distributions of S1', S1, and S2 under 5 mM NAM. Solid circles represent the experimental data. Solid curves represent simulated results averaged from 50 simulations, with shaded areas indicating standard deviation.

(E) Model-predicted single-cell state-transition trajectories of WT cells in response to the step input of 5 mM NAM at their 9th generation.

(F) Experimental state-transition trajectories of WT cells with the step input of 5 mM NAM after 600 min, when more than 70% of cells just enter their 9th generation.

(G) The lifespans of two aging paths in response to the dynamic perturbation. Predictions, red and blue curves; Experimental data, red and blue solid circles. Dashed curves are the lifespans for no NAM treatment and constant NAM treatment.

(H) Model-predicted age-dependent state distributions of S1', S1, and S2. Note the sharp increase of S1 and S2 at their 10th division (pointed by the red arrow). Solid curves are predictions averaged from 50 simulations, with shaded areas indicating standard deviation. Solid circles represent the experimental data.

See also Table S1.

sustained S1 or S2 state; therefore, if the sustained S1 state is induced earlier in life, the lifespan would be shortened. We set out to test whether our model can predict (without fitting parameters) the state-changing dynamics of an experiment, during which we artificially introduce the S1 state in the middle of the average WT lifespan.

To chemically induce the S1 state, we used nicotinamide (NAM), an inhibitor of Sir2. We had previously shown that cells exposed to 5 mM NAM largely resembled the phenotypic changes and aging dynamics of the *sir2Δ* mutant (Li et al., 2017), featuring an early occurrence of the S1 state. To quantify the S1 induction effect of NAM, we did control experiments in which cells are treated with constant 5 mM NAM and obtained transition rates from the data. The state-transition dynamics and lifespan with constant 5 mM NAM treatment are similar to those of *sir2Δ* (Figures 6A–6D).

With this information on NAM-driven S1 induction, we then let our model predict the aging dynamics when the S1 state is artificially induced in "middle-aged" WT cells. More specifically, the model generated predictions of state transitions and lifespan

distributions for a scenario where WT cells first age normally and then NAM is added to induce the S1 state at the 9th generation (Figure 6E; and curves in Figures 6G and 6H). The model predicted a sharp increase in the S1 state (also S2 state, though not as much as S1) (Figure 6E; and curves in Figure 6H) and a shortened lifespan that falls between that of normal aging and that of NAM treated from age zero (Figure 6G; curves).

To test the predictions, we performed a corresponding experiment in which 5 mM NAM was introduced to normally aging WT cells after 600 min, when about 71% of cells just entered the 9th generation, close to half of their normal RLS (21 generations). As shown in Figure 6F and dots in Figures 6G and 6H, the experimental data quantitatively matches the model predictions. This is significant in that based only on the rates inferred from the normal aging condition and the constant NAM-treated condition, our model can accurately predict dynamic perturbations, without fitting parameters or any additional assumptions.

These results validated our model and convincingly demonstrated its predictive power. Furthermore, the analysis of

CellPress

dynamic perturbations, such as the one presented here, can be used to shed light on mechanisms that drive the aging process.

DISCUSSION

Recent developments in microfluidics have enabled direct observations of phenotypic and molecular changes during aging at single-cell and molecular resolution, which will shed light on the mechanisms that drive single-cell aging (Chen et al., 2017). It nicely complements the traditional microdissection method, which measures lifespan as the primary readout, and provides important information about aging-related biological changes that result in the observed lifespan (Polymenis and Kennedy, 2012). Yet, an emerging challenge is to interpret newly available single-cell dynamic data to advance our understanding of the aging process. In this study, we developed a quantitative framework for analyzing the single-cell aging data. In particular, we defined distinct age-related cellular states from phenotypic changes and devised a stochastic model to describe heterogeneous state changes in individual aging cells with transition probabilities from single-cell data. We used this framework to investigate how and why isogenic cells age with different phenotypic changes and rates, a long-standing question in the biology of aging.

Cellular aging is associated with numerous molecular changes and damage accumulations (Crane and Kaeberlein, 2018). One scenario of the aging process is that individual cells end up with different causes of aging and death, simply depending on which molecular changes or damages dominate near the end of their lifespan. Therefore, stochasticity in the progression of and competition between different molecular changes or damage accumulation might underlie the heterogeneity in phenotypes and lifespans of genetically identical cells. Another possible scenario is that aging is a well-programmed process, with sequentially ordered molecular events leading to death. In this case, the heterogeneity might come from the variability in the kinetics between transition steps.

Our analysis revealed that the aging process is likely a combination of both scenarios: during the early phase of aging, at least two major molecular processes compete and result in two divergent aging paths. Once the decision has been made, a cell will proceed along the selected path, with characteristic phenotypic changes, toward cell death. The two paths are relatively irreversible as switching between the two paths rarely occurs. Hence, the two paths should be driven by distinct and sequentially programmed molecular processes leading to cell death. Previous studies suggested that one aging path characterized with elongated daughters (path 1) might be associated with a loss of chromatin silencing at the rDNA region (Li et al., 2017), whereas the other path with small round daughters and sharply extended cell-cycle lengths (path 2) might be related to mitochondrial dysfunction (Xie et al., 2012). A future systematic analysis of aging-related molecular markers is needed to elucidate the molecular basis of these aging paths.

Previous modeling studies of aging have focused primarily on specific molecular networks that drive deterministic population-level aging processes (Auley et al., 2015; Janssens et al., 2015; Kriete et al., 2010; Lorenz et al., 2009; Rodriguez-Brenes and Peskin, 2010; Wieser et al., 2011). Because of the scarcity of

aging-related data, very few of the studies were based on sufficient experimental data. Our model differs from previous studies in that it addresses the stochastic nature of cellular aging, focusing on the variability in single-cell aging dynamics, and it is supported by extensive single-cell data. The model is phenomenological and simple, considering only four discrete cellular states, but it effectively reproduces the observed dynamics and variability of phenotypic changes in isogenic cell populations. Moreover, it also provides crucial insights into the kinetics, history dependence, and divergence of single-cell aging trajectories. For example, the model reveals two reasons that contribute to the divergence in aging paths. One is due to a rapidly increasing transition probability from S1' and S1 to S1 ($p_{1'1}$, p_{11}) and a decreasing transition probability from S2 to S0 (p_{20}) during aging. Once a cell has transitioned to S1' or S2, it becomes unlikely to switch back to S0 and hence will stay in aging path 1 or 2. However, with only this mechanism at work, switching between the two paths would still be more frequent than that observed in experiments (Figure S4). The second cause of divergence comes from the history effect on transitions away from S0 in the early or middle phase of lifespan—the histories of most recent visits to S1'/S1 or S2 strongly bias the transition from S0 to the previously visited state, locking the cell into the path that is chosen in the early phase of lifespan.

Taking one step forward, we used our experimental and modeling approaches to analyze the effects of relevant genetic and environmental factors and obtained new insights on how these factors regulate the aging processes. Sir2, a well-studied deacetylase that controls chromatin silencing, stands as a proof-of-concept example in our studies. Our analysis of the single-cell data showed that Sir2 specifically regulates the state transitions in one of the aging paths (aging path 1, characterized with elongated daughters), linking this path as well as states S1' and S1 to the changes in the chromatin-silencing process. This is in accordance with previous molecular-level observations that a loss of chromatin silencing leads to the aging phenotype featured by the elongated daughter morphology (Li et al., 2017). It suggests that Sir2, by enhancing the intermittent dynamics of chromatin silencing, enables cells to switch back and forth between S0 and S1' states and hence impedes the progression of these cells along aging path 1 toward death, leading to an extended lifespan. We also pursued analysis of *SGF73*, the deletion of which drastically extends the lifespan through mechanisms significantly less well studied than *SIR2*. We found that in contrast to Sir2, which regulates a specific aging path, Sgf73 controls multiple different transition steps in both aging paths, consistent with previous biochemical results showing the pleiotropic functions of Sgf73 on many molecular processes (Denoth-Lippuner et al., 2014; Mason et al., 2017; McCormick et al., 2014). Moreover, although the two aging paths are mostly divergent in WT cells, we observed a larger fraction of *sgf73Δ* cells switch between the two paths, which suggests that the divergence in aging paths might represent a precisely regulated differentiation process, governed by molecular factors, such as Sgf73 or its substrate(s). The molecular mechanisms and physiological roles of this aging-dependent differentiation deserve further investigation. Finally, when applying our approach to examine the effects of CR, we found that CR biases cells toward

CellPress

aging path 1 and at the same time decelerates the cells' progression through aging path 1 to death. Previous studies showed that CR extends longevity through conserved nutrient-mediated kinases, including PKA, TOR, and Sch9 (Kaeberlein et al., 2005). Our analysis suggests that these kinases might regulate aging primarily through modulating molecular processes driving aging path 1, again setting the stage for the discovery of aging-critical phospho-proteins.

The analysis of the genetic and environmental perturbations we focused on uncovered a potential anti-aging role of a specific cellular state, S1', which is characterized by elongated daughter morphology and normal cell-cycle length. Whereas the short-lived *sir2Δ* mutant showed a reduced appearance of S1', the long-lived *sgf73Δ* mutant and CR both promoted the occurrence of this state during aging. We speculate that this state in some ways weakens the damage segregation barrier between mother and daughter cells. This will result in daughter cells with an abnormal morphology and probably a shortened lifespan but at the same time will temporarily relieve the mother cell from damage accumulation, thereby slowing its aging. Our previous study revealed a correlation between this phenotypic state with short-term losses of chromatin silencing or Sir2 activity (Li et al., 2017). For future studies, it would be interesting to test this damage-relief hypothesis and examine how Sir2 or chromatin silencing contributes to the process by monitoring intracellular damage molecules and phenotypic changes in the same aging cells in response to perturbations of Sir2 activity.

In this study, we integrated single-cell dynamic measurements with computational modeling and revealed the divergence of genetically identical cells along two major aging paths. The selection of the aging paths is tightly regulated by genetic and environmental factors, suggesting that cellular aging might be an actively regulated differentiation process rather than a passive damage-accumulation process. Our quantification and modeling efforts generated testable predictions that can guide future mechanistic studies. Furthermore, the phenomenological model we developed in this study could serve as a basic model for yeast aging, upon which more detailed, continuous, and mechanistic models can be built in the future.

STAR★METHODS

Detailed methods are provided in the online version of this paper and include the following:

- KEY RESOURCES TABLE
- CONTACT FOR REAGENT AND RESOURCE SHARING
- EXPERIMENTAL MODEL AND SUBJECT DETAILS
  - Strain Construction
- METHOD DETAILS
  - Time-Lapse Microfluidic Experiments
  - Quantification of Phenotypic Metrics
  - Computational Modeling

SUPPLEMENTAL INFORMATION

Supplemental Information can be found online with this article at https://doi.org/10.1016/j.cels.2019.02.002.

REFERENCES

Auley, M.T., Mooney, K.M., Angell, P.J., and Wilkinson, S.J. (2015). Mathematical modelling of metabolic regulation in aging. Metabolites *5*, 232–251.

Chen, K.L., Crane, M.M., and Kaeberlein, M. (2017). Microfluidic technologies for yeast replicative lifespan studies. Mech. Ageing Dev. *161*, 262–269.

Colman, R.J., Anderson, R.M., Johnson, S.C., Kastman, E.K., Kosmatka, K.J., Beasley, T.M., Allison, D.B., Cruzen, C., Simmons, H.A., Kemnitz, J.W., et al. (2009). Caloric restriction delays disease onset and mortality in rhesus monkeys. Science *325*, 201–204.

Crane, M.M., and Kaeberlein, M. (2018). The paths of mortality: how understanding the biology of aging can help explain systems behavior of single cells. Curr. Opin. Syst. Biol. *8*, 25–31.

Denoth-Lippuner, A., Krzyzanowski, M.K., Stober, C., and Barral, Y. (2014). Role of SAGA in the asymmetric segregation of DNA circles during yeast ageing. Elife *3*, https://doi.org/10.7554/eLife.03790.

Fontana, L., Partridge, L., and Longo, V.D. (2010). Extending healthy life span–from yeast to humans. Science *328*, 321–326.

Gartenberg, M.R., and Smith, J.S. (2016). The nuts and bolts of transcriptionally silent chromatin in *Saccharomyces cerevisiae*. Genetics *203*, 1563–1599.

Guarente, L., and Kenyon, C. (2000). Genetic pathways that regulate ageing in model organisms. Nature *408*, 255–262.

Harton, M.D., and Batchelor, E. (2017). Determining the limitations and benefits of noise in gene regulation and signal transduction through single cell, microscopy-based analysis. J. Mol. Biol. *429*, 1143–1154.

He, C., Zhou, C., and Kennedy, B.K. (2018). The yeast replicative aging model. Biochim. Biophys. Acta Mol. Basis Dis. *1864*, 2690–2696.

Henderson, K.A., and Gottschling, D.E. (2008). A mothers sacrifice: what is she keeping for herself? Curr. Opin. Cell Biol. *20*, 723–728.

Inaba, M., and Yamashita, Y.M. (2012). Asymmetric stem cell division: precision for robustness. Cell Stem Cell *11*, 461–469.

Janssens, G.E., Meinema, A.C., González, J., Wolters, J.C., Schmidt, A., Guryev, V., Bischoff, R., Wit, E.C., Veenhoff, L.M., and Heinemann, M. (2015). Protein biogenesis machinery is a driver of replicative aging in yeast. Elife *4*, e08527.

Kaeberlein, M., Powers, R.W., 3rd, Steffen, K.K., Westman, E.A., Hu, D., Dang, N., Kerr, E.O., Kirkland, K.T., Fields, S., and Kennedy, B.K. (2005). Regulation

of yeast replicative life span by TOR and Sch9 in response to nutrients. Science 310, 1193–1196.

Kennedy, B.K., Berger, S.L., Brunet, A., Campisi, J., Cuervo, A.M., Epel, E.S., Franceschi, C., Lithgow, G.J., Morimoto, R.I., Pessin, J.E., et al. (2014). Geroscience: linking aging to chronic disease. Cell 159, 709–713.

Köhler, A., Schneider, M., Cabal, G.G., Nehrbass, U., and Hurt, E. (2008). Yeast ataxin-7 links histone deubiquitination with gene gating and mRNA export. Nat. Cell Biol. 10, 707–715.

Kriete, A., Bosl, W.J., and Booker, G. (2010). Rule-based cell systems model of aging using feedback loop motifs mediated by stress responses. PLoS Comput. Biol. 6, e1000820.

Lakowski, B., and Hekimi, S. (1998). The genetics of caloric restriction in Caenorhabditis elegans. Proc. Natl. Acad. Sci. USA 95, 13091–13096.

Lee, K.K., Swanson, S.K., Florens, L., Washburn, M.P., and Workman, J.L. (2009). Yeast Sgf73/Ataxin-7 serves to anchor the deubiquitination module into both SAGA and Slik(SALSA) HAT complexes. Epigenetics Chromatin 2, 2.

Levine, J.H., Lin, Y., and Elowitz, M.B. (2013). Functional roles of pulsing in genetic circuits. Science 342, 1193–1200.

Li, Y., Jin, M., O'Laughlin, R., Bittihn, P., Tsimring, L.S., Pillus, L., Hasty, J., and Hao, N. (2017). Multigenerational silencing dynamics control cell aging. Proc. Natl. Acad. Sci. USA 114, 11253–11258.

Lorenz, D.R., Cantor, C.R., and Collins, J.J. (2009). A network biology approach to aging in yeast. Proc. Natl. Acad. Sci. USA 106, 1145–1150.

Mal, A.K. (2006). Histone methyltransferase Suv39h1 represses MyoD-stimulated myogenic differentiation. EMBO J. 25, 3323–3334.

Mason, A.G., Garza, R.M., McCormick, M.A., Patel, B., Kennedy, B.K., Pillus, L., and La Spada, A.R. (2017). The replicative lifespan-extending deletion of SGF73 results in altered ribosomal gene expression in yeast. Aging Cell 16, 785–796.

McCormick, M.A., Delaney, J.R., Tsuchiya, M., Tsuchiyama, S., Shemorry, A., Sim, S., Chou, A.C., Ahmed, U., Carr, D., Murakami, C.J., et al. (2015).

A comprehensive analysis of replicative lifespan in 4,698 single-gene deletion strains uncovers conserved mechanisms of aging. Cell Metab. 22, 895–906.

McCormick, M.A., Mason, A.G., Guyenet, S.J., Dang, W., Garza, R.M., Ting, M.K., Moller, R.M., Berger, S.L., Kaeberlein, M., Pillus, L., et al. (2014). The SAGA histone deubiquitinase module controls yeast replicative lifespan via Sir2 interaction. Cell Rep. 8, 477–486.

Mortimer, R.K., and Johnston, J.R. (1959). Life span of individual yeast cells. Nature 183, 1751–1752.

Partridge, L., Pletcher, S.D., and Mair, W. (2005). Dietary restriction, mortality trajectories, risk and damage. Mech. Ageing Dev. 126, 35–41.

Polymenis, M., and Kennedy, B.K. (2012). Cell biology: high-tech yeast ageing. Nature 486, 37–38.

Purvis, J.E., and Lahav, G. (2013). Encoding and decoding cellular information through signaling dynamics. Cell 152, 945–956.

Rodriguez-Brenes, I.A., and Peskin, C.S. (2010). Quantitative theory of telomere length regulation and cellular senescence. Proc. Natl. Acad. Sci. USA 107, 5387–5392.

Steffen, K.K., Kennedy, B.K., and Kaeberlein, M. (2009). Measuring replicative life span in the budding yeast. J. Vis. Exp. https://doi.org/10.3791/1209.

Steinkraus, K.A., Kaeberlein, M., and Kennedy, B.K. (2008). Replicative aging in yeast: the means to the end. Annu. Rev. Cell Dev. Biol. 24, 29–54.

Wieser, D., Papatheodorou, I., Ziehm, M., and Thornton, J.M. (2011). Computational biology for ageing. Philos. Trans. R. Soc. Lond. B Biol. Sci. 366, 51–63.

Xie, Z., Zhang, Y., Zou, K., Brandman, O., Luo, C., Ouyang, Q., and Li, H. (2012). Molecular phenotyping of aging in single yeast cells using a novel microfluidic device. Aging Cell 11, 599–606.

Yang, J., McCormick, M.A., Zheng, J., Xie, Z., Tsuchiya, M., Tsuchiyama, S., El-Samad, H., Ouyang, Q., Kaeberlein, M., Kennedy, B.K., et al. (2015). Systematic analysis of asymmetric partitioning of yeast proteome between mother and daughter cells reveals aging factors and mechanism of lifespan asymmetry. Proc. Natl. Acad. Sci. USA 112, 11977–11982.

STAR★METHODS

KEY RESOURCES TABLE

REAGENT or RESOURCE	SOURCE	IDENTIFIER
Experimental Models: Organisms/Strains		
BY4741 MATa his3Δ1 leu2Δ0 met15Δ0 ura3Δ0	S288C-derived strain	NH0256
BY4741 MATa his3Δ1 leu2Δ0 met15Δ0 ura3Δ0, NHP6a-iRFP-kanMX	Li et al., 2017	NH0268
BY4741 MATa his3Δ1 leu2Δ0 met15Δ0 ura3Δ0, RDN1::NTS1-P_{TDH3}-GFP, NHP6a-iRFP-kanMX	Li et al., 2017	NH0270
BY4741 MATa his3Δ1 leu2Δ0 met15Δ0 ura3Δ0, NHP6a-iRFP-kanMX, RDN1::NTS1-P_{TDH3}-GFP-URA3, sir2::HIS3	Li et al., 2017	NH0277
BY4741 MATa his3Δ1 leu2Δ0 met15Δ0 ura3Δ0, NHP6a-iRFP-kanMX, RDN1::NTS1-P_{TDH3}-GFP-URA3, sgf73::HIS3	Li et al., 2017	NH0465

CONTACT FOR REAGENT AND RESOURCE SHARING

Further information and requests for resources and reagents should be directed to and will be fulfilled by the Lead Contact, Nan Hao (nhao@ucsd.edu).

EXPERIMENTAL MODEL AND SUBJECT DETAILS

Strain Construction
Standard methods for the growth, maintenance, and transformation of yeast and bacteria and for manipulation of DNA were used throughout. The yeast strains used in this study were generated from the BY4741 (MAT a his3Δ1 leu2Δ0 met15Δ0 ura3Δ0) strain background.

METHOD DETAILS

Time-Lapse Microfluidic Experiments
Replicative aging experiments were performed using microfluidic devices following the design principles previously described and validated in Li et al. (2017). Relevant to the work described here, each single cell trap has a wider opening on the top (6 μm) and a slightly narrower (3 μm) opening at the bottom. The design of the trap allows the mother cell at the bottom to bud either upwards or downwards. If a daughter cell is budded from the top of its mother cell, it will be pushed out of the trap; if born at the bottom of a mother cell, the daughter cell will leave the trap from the bottom opening. This design feature allows daughter cells to be observed after they detach from their mothers and as long as a few cell cycles if they are born from the top. The limitation of this device is that we could not observe daughter cells long enough to determine their lifespan or final morphologies.

The microfluidic device was designed in AutoCAD (Autodesk Inc.). Modeling of fluid flow in the device using COMSOL Multiphysics aided in design (COMSOL Multiphysics® v.5.3. COMSOL AB, Stockholm, Sweden.). The cell trapping region of this device is 18 μm long, 6 μm wide and 4.3 μm high, with a 3 μm opening at the bottom. The media flow channel is 100 μm wide and 20 μm high. Each device contains 100 cell traps. Two chrome quartz glass masks (HTA Photomask), one for each layer of the device, were used to pattern SU-8 negative epoxy photoresist (MicroChem Corp.) onto clean silicon wafers (University Wafer Inc.). SU-8 2005 and SU-8 2015 (MicroChem Corp.) were used to build the cell trapping region and the media flow layer, respectively.

Yeast cells were inoculated into 2 ml of synthetic complete medium (SC, 2% dextrose) and cultured overnight at 30°C. 2 μl of saturated culture was diluted into 20 ml of fresh SC medium and grown at 30°C overnight until it reached OD600$_{nm}$ ~ 1.0. For loading, cells were diluted by 10-fold and transferred into a 60 ml syringe (Luer-Lok Tip, BD) connected to plastic tubing (TYGON, ID 0.020 IN, OD 0.060 IN, wall 0.020 IN). For WT, sir2Δ, and sgf73Δ experiments, SC medium with 2% dextrose and 0.04% Tween 20 was used. For caloric restriction experiments, SC medium with 0.05% dextrose and 0.04% Tween 20 was used.

Since the experiments studied the aging dynamics from the beginning to the end of a cell's lifespan, it is important to ensure that cells loaded in our device indeed start from the beginning of their lifespans. To make sure only new born mother cells are loaded into traps, we consistently use cell culture at exponentially growing phase (confirmed in Li et al. [2017]). In exponentially growing cultures, 50% cells are just born, 25% just divided once, 12.5% divided twice, 6.25% divided three time, etc. Thus, 93.5% cells have only divided no more than three times.

Time lapse microfluidic experiments were conducted as described in Li et al. (2017). In brief, devices were vacuumed for 20 min before imaging, and primed with 0.075% Tween 20 (Sigma-Aldrich Co.) for 5 min after vacuuming. Media ports were connected to 60 ml syringes with fresh medium with 0.04% Tween-20 via plastic tubing (TYGON, ID 0.020 IN, OD 0.060 IN, wall 0.020 IN). The waste ports were connected to a 50ml Falcon tube. A 60-inch-height difference between medium and waste was set to allow a flow rate (measured by amount of waste medium collected during experiments) of about 2.5 ml/day for all experiments.

Quantification of Phenotypic Metrics

Phase contrast images from microfluidic experiments were used for quantification. Daughter cells were fit to ellipses with the elliptic selection tool in ImageJ (Rasband, W.S., ImageJ 1.49v, National Institutes of Health, Bethesda, Maryland, USA, https://imagej.nih.gov/ij/, 1997-2018.) and both the area and aspect ratio of corresponding elliptic fits were measured using ImageJ. For each daughter cell, these metrics were measured consistently at the time frame immediately after the daughter cell was completely separated from the mother. The area of mother cells was measured in the same way at the same time point. Each cell division was identified and counted at the time frame when a bud was first observed in the mother. The time between two adjacent cell divisions of the mother cell is defined "Cell-Cycle Length".

The threshold for aspect ratio (0.6) comes from the minimum between the two peaks in the aspect ratio – daughter/mother area ratio space (Figure 1C, left panel) along the aspect ratio axis. The threshold for daughter/mother area ratio (0.5) is chosen such that all cells with daughter aspect ratio <0.6 will stay above this threshold, and that cells with high daughter/mother area ratios stay orthogonal to the S1/S1' area (a.k.a. cells with small daughter aspect ratio). The thresholds for aspect ratio and daughter/mother area ratio are drawn as the black lines in Figure 1C, left panel. The cell cycle threshold is chosen by the difference in the distributions of cell-cycle duration for those in S0 area and those in S2 area and S1 area. The threshold of cell cycle is drawn as the black line in Figure 1C, right panel.

We systematically performed sensitivity analysis for threshold values to confirm whether the quantitative effects of mutants ($sir2\Delta$ and $sgf73\Delta$) and the growth condition (0.05% glucose) on various transition rates (Figures 3D, 4E, and 5D) still hold (Figure S8). The thresholds were varied within a -15% to 15% range at 5% intervals from the current chosen values. We varied the aspect ratio threshold (0.6) in the range of [0.51 0.54 0.57 0.6 0.63 0.66 0.69], the daughter/mother area ratio threshold (0.5) in the range [0.425 0.45 0.475 0.5 0.525 0.55 0.575] and cell cycle threshold (125%) with [106% 112% 118% 125% 131% 137% 143%] increase from the mean T_{early}. For each threshold change, we calculated transition rates in all experiments, and compared specific transition rates of interest: $p_{01'}$, p_{01} and p_{1D} between WT and $sir2\Delta$ cells, $p_{1'0}$, p_{20}, p_{2D} between WT and $sgf73\Delta$ cells, and p_{01}, $p_{1'0}$, p_{1D} between WT and CR treated cells (Figure S8). Since the same transition rates are defined for different ranges of replicative age in different experiments, it is not immediately obvious how to compare them directly (such as Figure S8A). For a fair comparison, we therefore calculated the "total transition probability", $P_{ij} = \dfrac{\sum_{k=1}^{\infty} n_{S_i \to S_j}^{k}}{\sum_{k=1}^{\infty} n_{S_i}^{k}}$, k=1, ..., last generation, which is independent of the typical lifespan.

Compared with WT cells, $P_{01'}$ remained smaller, P_{01} and P_{1D} are higher in $sir2\Delta$ cells for all 3 sets of thresholds we tested (Figures S8B–S8D). $sgf73\Delta$ cells kept higher $P_{1'0}$, P_{20} but smaller P_{2D} compared with WT cells (Figures S8E–S8G). CR consistently led to P_{01} and $P_{1'0}$ higher than those of WT cells, and lowered P_{1D} (Figures S8H–S8J). Our conclusions about the effects of different mutants and growth conditions on state transition dynamics therefore hold within the range of tested thresholds.

Computational Modeling

Our state transition model makes several assumptions: (1) mother cells start from state S0 and can exist in any one of the four states; (2) cells transition from one state to another with transition probabilities per cell division that are functions of replicative age; (3) the most recent visits to states S1'/S1 and S2 affect the transition probability from S0 to S1', S1 and S2; and (4) if mother cells are in state S1 or S2, they have a certain probability to die, and the transition probability from S1 or S2 to death are a function of the number of continuous cell divisions in either S1 or S2 state.

Transitions between states are purely stochastic and are characterized by transition probabilities p_{ij} (i,j=0,1',1,2) that depend on the replicative age of mother cells. To estimate these transition probabilities from single-cell data, we computed the fraction of all the cells at the state i (i=0, 1', 1, 2) of a given generation that switch to the state j (j=0, 1', 1, 2) at the next cell division for all available generations. As experimental data shows, the transition probabilities change linearly with cell division number (replicative age), though these rates fluctuate strongly when the incidences of transitions are low (Figures S2 and S5–S7). Using linear regression of the data, we approximate the dependence of p_{ij} at replicative age N by linear functions. The transition probabilities are fit by weighted linear least squares with metropolis sampling, where the weight is the square root of the number of cells which underwent the corresponding state transitions at a given generation N (Figures S2 and S5–S7). Transition probabilities are grouped into 6 sets: 3 sets for p_{0j} (j=0,1',1,2) with three history conditions (see below for details), 1 set for $p_{1'j}$ (j=0,1',1), 1 set for p_{1j} (j=0,1',1), 1 set for p_{2j} (j=0,2). Since transition rates represent probabilities per generation, they are capped at 0 and 1. If a transition rate, p_{ij}, hits the cap at any generation N, then all rates describing transitions originating from the same state i, p_{ik}(k≠j), are kept at their current values for all generations following generation N. The transition rates in each of the six sets are fit simultaneously with the constraint that the sum of them equals 1. The error bar of transition probability p_{ij} at generation m (m=1, 2, 3, …) is the expected standard deviation, since we only have one dataset for each condition (each dataset contains 2-3 experiments to include more than 150 cells). For transition Si->Sj at division m, the expected standard deviation is calculated as the square root of ($p_{ij}(1-p_{ij})/N$), where p_{ij} is the transition probability and

N is the total number of cells in state Si at division m. This corresponds to the expected variability of p_{ij} due to the limited number of cells in our experiments, assuming that p_{ij} is the true transition probability. This variability is inherent to binomial sampling of cells in state Si, where success is defined as a transition to Sj. When $p_{ij} = 1$ or 0, we use the square root of (1/N) to be conservative. Similarly, the error bars of switching frequency between paths are calculated in the same manner, as the "expected standard deviation", indicating the uncertainty due to the limited number of cells, inherent to the nature of the experiments.

For transitions from state S0 to S0, S1', S1 and S2, we further distinguish them based on whether a mother cell currently in state S0 has experienced S1', S1 or S2 states before. This history dependence is equivalent to introducing two additional hidden states of S0 into the model: one is an S0 state where a cell enters after most recently visiting S1' or S1 state (other than S2 state), the other is an S0 state where a cell enters after most recently visiting S2 state (other than S1' or S1 state). We took the history into consideration because simulations without this differentiation consistently over-estimate the amount of cells switching between aging path 1 and path 2. That is, more trajectories switch to S2 state before they finally commit in S1 state, and vice versa (Figure S4). For the effect of history, we calculated three sets of transition rates from S0: one for cells with no history in states S1', S1 or S2 (i.e. which have never left state S0); one for cells whose most recent excursion from S0 was to states S1' or S1; and one for cells whose most recent excursion from S0 was to state S2. The history between S1' and S1 are not further distinguished, since it is not necessary to reproduce the experimental data.

Based on the observation that almost all cells died after consecutive cell divisions in state S1 or S2, we postulate that cellular damages accumulate continuously in these states, and that the probability to die increases with the number of consecutive generation in either state. To estimate probabilities to cell death, we calculated the probability to die from S1 or S2 by the fraction $f_{Si \rightarrow D}$ (i=1, 2) of cells that died after M consecutive generations in S1 or S2 to total number of cells that lived through M consecutive generations of S1 or S2. Evidently, this fraction increases with M until it reaches 1; meanwhile it becomes much noisier since the number of cells satisfied these conditions decreases drastically. We fit this ratio for all experiments to the simplest polynomial functions possible (Table S1; Figure S3). For WT and *sgf73Δ* cells, the best fits are second-order polynomials; for *sir2Δ* and caloric restriction cells, first-order polynomials fit well.

Thus, this phenomenological model depends on state transition rates and death rates. Time unit in simulations is one generation/cell division. We simulated this model stochastically and in each *in silico* experiment we generated the same number of mother cell trajectories as in the experiment with the corresponding cell type or condition. Averaging over 50 *in silico* experiments for all experiments, we computed the fraction of cells in each state as a function of their replicative age N and the faction of cells alive at replicative age N as a function of M. The shaded regions in Figures 2E, 2F, 3B, 3C, 4B, 4C, 5B, and 5C indicate standard deviations of the corresponding metrics from multiple runs, showing that the simulations faithfully reproduce the experimental data. We also plotted a set of individual cell state trajectories from one run ordered by their replicative lifespan (Figures 2D, 3A, 4A, and 5A).

To check whether linear approximation for transition probabilities between S0, S1', S1 and S2 is necessary, we tested a model that assumes of constant transition rates. We found the best constant fits for transition probabilities between the four states, and then performed simulations with these best fits for all four experiments. The best simulations using constant transition rates deviated greatly from the state distributions and survival curves of the experimental data (Figure S9, compared to Figures 2, 3, 4, and 5), justifying the use of linear approximations for the transition probabilities. We also tested the linear approximations for the transition probabilities to death for WT and *sgf73Δ* cells (simpler than the second order polynomials approximations used in the main text). In both cases, the survival rates from simulations deviated more from the data compared with simulations using second order polynomial fits (Figure S10, compared to Figures 2E and 4B). We calculated the mean square distance (msd) between simulations and the data to compare the linear vs second-order polynomial assumptions of death probability. For WT, the msd for survival rates are 2- and 3-fold of those in Figure 2E for Path 1 and Path 2, respectively. For *sgf73Δ* cells, the msd for survival rate is 3-fold of that in Figure 4B for Path 2, and comparable to that in Figure 4B for Path 1.

Simulations and plots were generated using MATLAB (MATLAB and Statistics Toolbox Release 2015a, The MathWorks, Inc., Natick, Massachusetts, United States). The code from this work is available at GitHub https://github.com/MengJ-bioDyn/aging_model_statetrans.